Development of a Portable and Low-Cost Data Acquisition System with Edge Intelligence for Electrical Impedance Tomography-Based Spatial Damage Detection

Damond M. Li and Long Wang

Abstract— Electrical impedance tomography (EIT) is a noninvasive imaging technique that can inspect the internal conductivity distribution of a material of interest. Currently, to perform continuous anomaly monitoring measurement data needs to be constantly streamed to an external device (e.g., a computer) for analysis. This can be highly energyinefficient, especially for a deployable, battery-powered EIT data acquisition (DAQ) system. To transform the conventional workflow and advance the EIT technique, this study developed an edge intelligence functionality for a novel, portable, low-cost, and wireless EIT DAQ system, enabling the DAQ hardware to detect the existence of anomalies. This study also demonstrated that future research could focus on addressing hardware limitations to further improve EIT reconstruction resolution on edge devices. Overall, this study laid the foundation for advancing EIT DAQ systems to include edge intelligent functionality so that they can operate independently from any external devices for continuous monitoring applications.

Index Terms— Compressed sensing, data acquisition system, edge intelligence, electrical impedance tomography, spatial damage detection

I. INTRODUCTION

LECTRICAL impedance tomography (EIT) is an imaging technique that aims to characterize the spatial conductivity distribution in a medium using electrical voltage measurements performed along the boundary [1, 2]. In recent decades, the EIT technique has attracted extensive attention due to its unique capability in non-destructive, non-radioactive, and distributed detection of anomalies in the materials of interest, making it ideal for various applications in medical imaging and structural health monitoring (SHM). For instance, the EIT technique has been used in early diagnosis of tumors [3-5], wearable/implantable technologies [6-9], monitoring of lung ventilation [10-12], monitoring of brain activity [13-15], and identifying human body positions [9], [16], [17]. In addition, in the context of SHM, the EIT technique has been demonstrated promising for identifying

Damond M. Li is with the Mechanical Engineering Department at California Polytechnic State University, San Luis Obispo, CA, 93407, USA.

Long Wang is with the Civil and Environmental Engineering Department at California Polytechnic State University, San Luis Obispo, CA, 93407, USA (e-mail: lwang38@calpoly.edu).

impact damage and delamination in carbon fiber-reinforced composites [18-21], and monitoring crack development in concrete [22-25].

A. Existing Portable EIT Data Acquisition Systems

Multiple large-scale and expensive instruments are often required to perform high-quality EIT measurements, which has significantly hindered broader applications of EIT. Many research endeavors have been reported to develop low-cost EIT data acquisition (DAQ) systems that are more portable with smaller spatial footprints, such as the Tomo [9] and the Spectra EIT [26]. The Tomo is an 8-electrode wearable EIT DAQ system that supports 2-pole measurements designed for detecting various hand gestures. The Tomo system was later advanced to support 32 electrodes with both 2-pole and 4-pole measurements [27]. Both Tomo systems are low-cost (\$40 for [9] and \$80 for [27]) and have small spatial footprints of $\sim 7 \times$ 4 × 3 cm³. Another device, Spectra EIT, is a portable 32electrode EIT DAO system that also supports 2- and 4-pole measurements with a spatial footprint of $\sim 5 \times 5 \times 3$ cm³. Additional features of Spectra EIT include external battery support and Bluetooth Low Energy wireless communication. While all of these systems have demonstrated excellent EIT measurement performance, they share a common limitation that is the reliance on external computation to process their measurements (i.e., hand gesture classification, conductivity reconstruction, etc.), which constrains broader applications of the EIT technique. Therefore, this study aims to address this by implementing a form of edge intelligence onto the EIT DAQ hardware.

B. Edge Intelligence/Computation

Recently, there have been increasingly more endeavors to decentralize and shift computation closer towards the "edge". This became possible due to hardware advancements that render edge devices more powerful and capable of such computation. Benefits of edge computation include reduced latency, reduced computation demands from the central processing device, and improved reliability [28]. For example, it may be preferable for an autonomous vehicle to make inferences at the edge (i.e., on-board the vehicle) rather than relying on some form of external computation, such as a centralized data processing center. If the connection to the processing center were unstable, it could be a serious safety

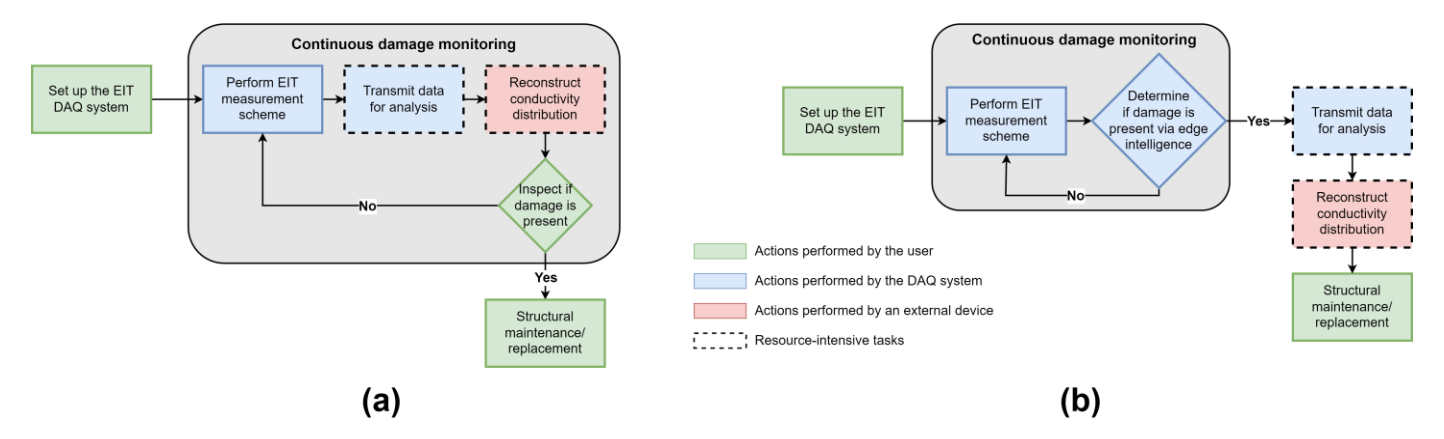


Fig. 1. (a) Workflow diagram of the conventional method applying EIT for SHM. (b) Workflow diagram proposed in this study by implementing a novel EIT DAQ system with edge intelligence for SHM.

hazard. By the same token, latency can be improved for timesensitive applications since the data does not have to travel far to be processes. Thus, the goal of this study is to advance the EIT DAQ systems through developing a novel edge intelligence capacity for the EIT DAQ hardware, which will fundamentally avoid the reliance on centralized external computation. This study lays the foundation for implementing the EIT technique for structural health monitoring applications (e.g., onboard damage sensing for aerospace structures), where centralized computation is inaccessible or limited.

C. Transforming EIT Workflow for Applications

Fig. 1(a) outlines a conventional workflow of applying the EIT technique for detecting structural damage by monitoring the spatial conductivity of structural materials. To be specific, the workflow generally consists of setting up the DAQ system, performing an EIT measurement scheme, transmitting measurements to an external device for data analysis, and inspecting for anomalies which is performed by the operator. In this workflow, data must be continuously transmitted to an external device for data processing and conductivity reconstruction. From the SHM standpoint, structural damage, especially crucial damage, may develop in an unpredictable manner, making large amounts of the data transmitted redundant (i.e., not containing any significant anomalies). For a deployable, battery-powered, and wireless DAO system, transmitting redundant data can be highly energy-consuming, which can fundamentally limit the long-term operation of the DAQ system. Alternatively, if the DAQ system itself can identify anomalies in the material of interest, measurement data can then be selectively transmitted to the external device for further analysis, which can be a promising approach to save energy and prolong battery life.

To transform the traditional workflow of EIT-based damage monitoring, this study aims to establish a novel workflow that shifts the resource-intensive tasks outside of the continuous monitoring stage, as shown in Fig. 1(b). In this study, a novel, portable, and low-cost EIT DAQ system has been developed, which incorporated edge intelligence function to enable the DAQ system to replace the external device and perform on-board reconstruction of spatial conductivity. In addition to the

edge intelligence functionality, this system supports 32 electrodes, 2- and 4-pole measurements, external lithium-polymer batteries, and Bluetooth Low Energy for wireless communication. With data analysis performed on the DAQ hardware, it has the ability to selectively transmit only the dataset that contains potential anomalies for further analysis and/or alert the users. While the concept of implementing edge intelligence onto EIT DAQ systems was also mentioned in [29], their work still relied on external computation, rather than the DAQ itself, to process the measured data. To our knowledge, our work represents the first successful attempt in achieving edge intelligence capacity for EIT DAQ systems and directly performing onboard EIT reconstructions using the DAQ hardware itself.

It is envisioned that the DAQ system developed in this study can significantly advance the applications of the EIT technique in the SHM of civil and aerospace structures as well as wearable technologies (e.g., for sensing prosthetics and human-machine interfaces).

D. Outline of the Paper

This paper first outlines the theoretical background of the EIT algorithms, followed by a detailed description of the design for a wireless, portable, battery-powered, and low-cost EIT DAQ hardware as well as the encoded EIT measurement scheme. Then, the paper demonstrates a set of benchmark tests conducted to evaluate the DAQ hardware performance. The paper also discusses the coupling of the DAQ system and EIT inverse algorithms for detecting and spatially locating damages (i.e., anomalies) in a conductive material. Finally, the edge computing capacity of the DAQ system is evaluated, followed by a discussion of its advantages and limitations as well as an outlook for future research.

II. EIT BACKGROUND

EIT algorithms typically include two parts, namely forward problem and inverse problem [2], [30], [31].

A. Forward Problem

The EIT forward problem attempts to solve for the boundary voltages of a medium (v) based on an assumed

conductivity (σ) distribution [32]. Assuming no current sources or sinks are present in the medium of interest (Ω), the forward problem can be formulated as

$$\nabla \cdot (\sigma \nabla v) = 0 \quad in \, \Omega \tag{1}$$

which is also known as the simplified 2D Laplace equation [30, 32]. Solving the forward problem typically involves combining (1) with a finite element model of the conductive body into a set of linear equations [30] expressed in the form of

$$A(\sigma)b = I \tag{2}$$

where $A(\sigma)$ is an invertible square matrix, representing a discretized expression of the complete electrode model, and I is the injected current. b is a coefficient vector that is to be solved for, which contains the elemental nodal potentials and the boundary electrode voltages.

B. Inverse Problem

On the other hand, the EIT inverse problem attempts to reconstruct the spatial conductivity distribution using the measured boundary voltages. Solving the inverse problem generally involves minimizing the difference between the estimated boundary voltages and the actual measurements:

$$\min_{\sigma} \left\| \delta V_{\partial\Omega}^{measured} - \delta V_{\partial\Omega}^{\sigma^*} \right\|^2 \tag{3}$$

where σ^* is the estimated conductivity, $\delta V_{\partial\Omega}^{\sigma^*}$ is the estimated voltages at the boundary corresponding to σ^* , and $\delta V_{\partial\Omega}^{measured}$ is the actual boundary voltage measurements [31].

As the EIT inverse problem is ill-posed [2], [30], [33], different optimization algorithms have been implemented to stably reconstruct the conductivity distribution. For instance, one of the most common methods is an iterative Gauss-Newton algorithm that uses the L_2 -norm as the regularization term, as expressed in (4):

$$\delta\sigma = \operatorname{argmin} \frac{1}{2} \|J\delta\sigma - \delta V\|_2 + \frac{\alpha}{2} \|L\delta\sigma\|_2 \tag{4}$$

where J is the Jacobian matrix, $\delta\sigma$ is the change in spatial conductivity within the medium, and δV is the measured change in boundary voltages. α is the regularization parameter and L is the regularization matrix, often formulated as an identity matrix I [30]. Equation (4) solves for $\delta\sigma$ by minimizing the difference between δV and $J\delta\sigma$ (i.e., mapped changes in the boundary voltages). The solution to the linearized regularization problem can then be obtained as

$$\delta\sigma = (J^T J + \alpha I)^{-1} J^T \delta V \tag{5}$$

C. Compressed Sensing Technique

To improve the reconstruction resolution and accuracy, another approach is based on the compressed sensing technique, which leverages the spatial sparsity of typical EIT problems [30], [31], [34]. In the context of compressed

sensing-based reconstruction, the objective function of the inverse problem becomes:

$$\delta\sigma = argmin \frac{1}{2} \|J\delta\sigma - \delta V\|_2 + \lambda \|\delta\sigma\|_1 \tag{6}$$

where λ is the regularization parameter, and $\|\delta\sigma\|_1$ is the L₁-norm of $\delta\sigma$ [30]. This study focused on implementing the compressed sensing technique for the EIT inverse problem and adopted a two-step iterative shrinkage thresholding (TwIST) algorithm [30], [31], [35] to robustly solve (6). The main equations in the modified TwIST algorithm takes the form of:

$$\delta\sigma_1 = \varphi_\lambda(\delta\sigma_0 + J^T(\delta V - J\delta\sigma_0)) \tag{7}$$

$$\delta\sigma_{t+1} = (1 - \alpha)\delta\sigma_{t-1} + (\alpha - \beta)\delta\sigma_t + \beta\varphi_{\lambda}(\delta\sigma_t + J^T(\delta V - J\delta\sigma_t))$$
(8)

where α and β are weight hyperparameters, and φ_{λ} is the soft thresholding function [30]. Note that $\delta \sigma_{t+1}$ is dependent on previous iterations $\delta \sigma_t$ and $\delta \sigma_{t-1}$, which is why the algorithm contains two steps. The soft thresholding function, φ_{λ} , takes the form of:

$$\varphi_{\lambda}(\delta\sigma_{t},\lambda) = sign(\delta\sigma_{t})max(|\delta\sigma_{t}| - \lambda,0)$$
 (9)

More details about the TwIST algorithm and its EIT implementation can be found in [35] and [30], respectively. Both the Gauss-Newton algorithm and the compressed sensing TwIST algorithm were coupled with the designed DAQ hardware to compare their reconstruction performance.

III. EXPERIMENTAL DETAILS

A. Data Acquisition Hardware Development

The EIT DAQ system consisted of four main components, namely, a constant current source, an array of switches/multiplexers, an analog-to-digital (ADC) converter to measure the voltages, and a controller to switch the multiplexer channels. Fig. 2 shows a schematic diagram that outlines the major components of the DAQ system and their interactions.

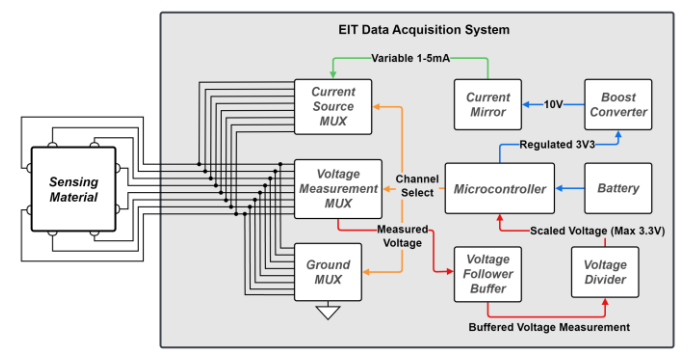


Fig. 2. Schematic diagram of major components in the DAQ hardware.

As shown in the schematics, the microcontroller was powered by an external battery and the regulated 3.3 V was

boosted up to 10 V to power the current mirror (i.e., the constant current source). All the channel-select signals from the multiplexers were controlled by the microcontroller. The output channels from each multiplexer were connected to the sensing material. Voltages were buffered and scaled before connecting to the ADC on the microcontroller. Fig. 3 exhibits the physical layout of the assembled DAQ hardware, and the design of its components are described in detail. Overall, the cost of the entire DAQ hardware was estimated to be ~ 80 US Dollars.

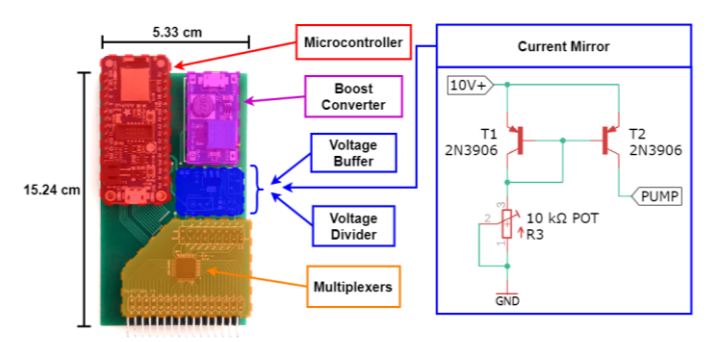


Fig. 3. Physical layout of an assembled DAQ system with each major component labeled.

- 1) Microcontroller: An Adafruit Feather nRF52840 Express was chosen to serve as both the controller and the ADC. The nRF52840 Feather board has a small physical footprint (5.08 × 2.29×0.71 cm³), a built-in 2-pin Japan Solderless Terminal (JST) PH series connector that supports any 3.7V LiPo batteries, and Bluetooth Low Energy (BLE) 5.0 for wireless communication [36]. There are also 21 general purpose input/output (GPIO) pins on the nRF52840 Feather, which were enough to support the three 32-channel multiplexers used in this study. The nRF52840 also features one of the largest memory capacities for a microcontroller (1024 kB of flash memory) which was deemed crucial for our application. Other microcontroller development boards either lacked desired features (i.e., Bluetooth support, sufficient GPIO pins, JST connector, etc.) or were known for having non-linear analogto-digital converters which would negatively hinder voltage measurements.
- 2) Multiplexers (MUX): The ADG732 MUX is commonly used for battery-powered systems, data acquisition systems, as well as medical instrumentation [37]. A total of three MUXs were utilized to perform the adjacent EIT measurement scheme. In particular, two MUXs formed the adjacent current injection pair, and the third MUX measured the voltages relative to the ground. The voltages measured relative to ground were then processed via customized code to attain the adjacent voltage measurements.
- 3) Constant Current Source: To obtain accurate boundary voltage measurements, it is important for the EIT DAQ system to inject a controllable and constant electrical current to the medium of interest. The current source was a current mirror made of two 2N3906 bipolar PNP transistors. A 10 k Ω trimmer potentiometer was used to control the reference current that was then mirrored across to the conductive

material of interest. The regulated 3.3 V output from the nRF52840 was passed through an MT3608 boost converter up to 10 V to power the current source.

- 4) Analog-to-digital Converter: The built-in ADC in the nRF52840 was utilized to measure the voltages at each electrode. With 10 V powering the current source coupled by the fact the voltages were measured relative to the ground, it was inevitable that the measured voltages exceeded the allowable 3.3 V input into the ADC. To address this challenge, a voltage divider, implemented with a 10 k Ω potentiometer, scaled the measured voltages down to a maximum of 3.3 V. To ensure minimal current draw when connecting each electrode to the ADC, an OPA810 rail-to-rail op-amp, configured as a voltage follower, was placed before the voltage divider to act as a voltage buffer.
- Bluetooth-based Wireless Communication: 5) The nRF52840 Feather board supported the BLE module, which enabled wireless connectivity between the microcontroller and another Bluetooth transceiver (e.g., smartphone). The Bluefruit Connect app from Adafruit Industries was used to connect to and operate the DAQ system via the BLE Universal Asynchronous Receiver/Transmitter (UART) protocol. The UART protocol was chosen over the BLE Generic Access Profile (GAP) and the Generic Attribute Profile (GATT) protocols for compatibility with the interactive controller in the Bluefruit Connect smartphone app [38], [39]. It should be noted that the DAQ hardware was operated wirelessly using a smartphone to perform all the experimental measurements in this study.

B. EIT Measurement Scheme

The current injection method used in this study was the adjacent current driving mode. To be specific, two adjacent electrodes were selected to be the driving electrodes, where one was used to inject the current into the conductive material of interest and the other was grounded for current to flow out. The voltages across all adjacent electrodes were measured and recorded with the measurements involving the driving electrodes omitted [40]. This process was repeated for all adjacent pairs of electrodes. The total number of measurements for this driving mode can be calculated by

$$M = N(N-3) \tag{10}$$

where M represents the number of measurements in each set and N represents the number of electrodes. For instance, a 16-electrode setup will yield a total of 208 measurements.

To further illustrate the measurement scheme, Fig. 4 shows an 8-electrode configuration as an example. The labels E0-E7 refer to electrodes 0-7, and P0-P7 refer to electrode pairs 0-7. E0 is the upper-leftmost electrode, and each electrode is positively indexed clockwise. If the sample is circular rather than quadrilateral, E0 corresponds to the topmost electrode with the rest of the electrodes indexed clockwise. The first electrode pair P0 is between E0 and E1 which also positively indexes clockwise.

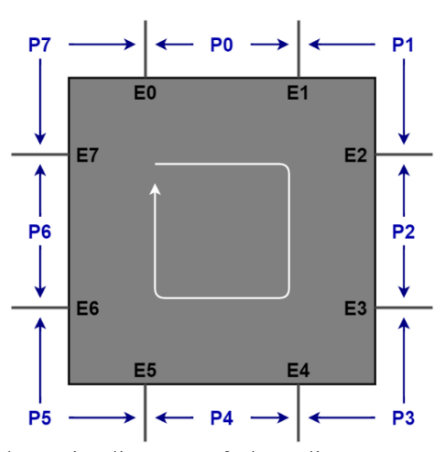


Fig. 4. Schematic diagram of the adjacent current driving mode measurement scheme used in this study.

During the measurement, current flows from E1 to E0 for the first injection pattern, E2 to E1 for the second, and so on. In this study, for each injection pattern, measurements were always taken starting with P0 (i.e., measuring the voltage drop from E0 to E1) through to P7. This measurement protocol also applied to other electrode configurations (e.g., 16- and 32-electrode setups).

C. Benchmark Testing of the DAQ System

1) Comparison with Circuitry Simulation: To evaluate the measurement accuracy of the designed DAQ hardware, a network of known resistors was fabricated and simulated using the LTSpice software. Fig. 5(a) and 5(b) show a diagram of the resistor network and its physical model, respectively.

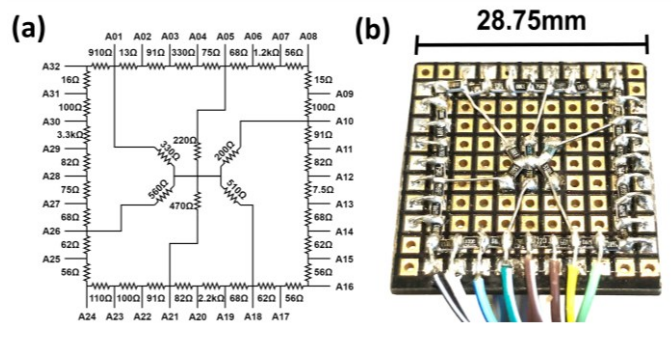


Fig. 5. (a) Schematic diagram of the resistor network for benchmark testing. (b) Optical image of the fabricated resistor network corresponding to (a).

To implement the DAQ hardware for measuring the resistor network, one electrode was connected to the current source, another electrode was connected to ground, and voltage measurements were taken across all electrodes. As the injection and ground electrodes altered, the equivalent resistance across the current source would also vary. Therefore, the performance of the current source could be tested by observing how the voltage measurements change under different loads. In addition, the DAQ accuracy would be evaluated by comparing the voltage measurement at each

electrode with the simulated values obtained from the LTSpice software.

2) Characterization of Measurement Noise and Signal Processing: Another aspect of the DAQ system performance evaluated was the level of noise in the measurements that may be induced by the ADC or current source. First, in a similar configuration described in Section III.C.1, the voltage at an electrode was repeatedly measured and recorded at a fixed sampling rate of about 500 samples per second. The recorded values were then used to calculate the covariance and the signal-to-noise ratio. A scalar Kalman filter was tuned with the calculated signal covariance to further improve measurement quality [41-43].

D. Application of the DAQ System for EIT Experiments

- 1) Materials: In this study, the designed DAQ system, coupled with the EIT algorithms, was implemented to detect damage on electrically conductive materials. Here, conductive carbon-filled ultra-high molecular weight polyethylene (UHMWPE) purchased from McMaster-Carr (thickness: 0.127 mm; surface resistivity: $10^3~\Omega/\text{sq.}$) was used as the material of interest for the EIT experiments. To establish boundary electrodes on the conductive UHMWPE, fast-drying conductive silver paint and two-ply conductive threads were acquired from Ted Pella and Adafruit, respectively.
- 2) Sample Fabrication: The UHMWPE sheets were first cut into $15 \times 15 \text{ cm}^2$ squares for the 16-electrode samples. Fig. 6 shows the schematic diagram of a representative edge with boundary electrodes for the 16-electrode samples.

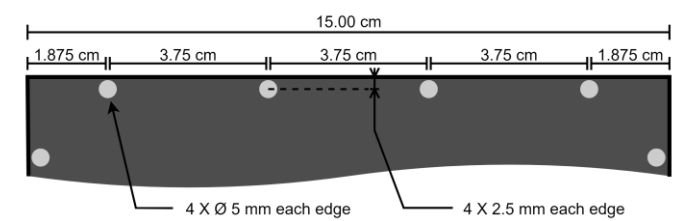


Fig. 6. Schematic diagram of a representative edge on a 16-electrode sample with four electrodes on each side for illustrating the spacings of boundary electrodes.

In particular, electrodes were positioned ~ 3.75 cm apart as close to the edge as possible. The outermost electrodes were positioned ~ 1.88 cm away from the adjacent edges. The boundary electrodes were established by air-drying silver paint on conductive threads for at least 30 min before testing. The contact region between each electrode and the UHMWPE sheets was ~ 5 mm in diameter. Furthermore, in this study, 8-electrode samples were also fabricated following similar procedures and were utilized to characterize the edge computing performance of the DAQ system. It should be noted that for the 8-electrode configuration, the UHMWPE sheets were cut into 7.5×7.5 cm² squares maintaining the same electrode spacing shown in Fig. 6.

3) EIT-based Damage Detection Experiments: To conduct the tests, the DAQ hardware was first connected to the electrodes on the UHMWPE samples using alligator clips.

Then, the DAQ system was commanded wirelessly via Bluetooth to perform the EIT measurement scheme on the undamaged samples, which established baselines for the initial conductivity distribution. These baselines were compared to their theoretical values obtained from the EIT forward problem solved with the Electrical Impedance Tomography and Diffuse Optical Tomography Reconstruction Software (EIDORS), an open-source software package written in MATLAB primarily for EIT [44]. The forward problem model was set up as a 16-electrode system with a uniform conductivity distribution and was discretized into a 96 × 96 finite element mesh. By solving the forward problem on the model using the adjacent current driving mode, theoretical boundary voltage distributions were obtained to compare with the experimental measurements. Anomalies (i.e., damages) were then introduced in the form of holes (~ 6.4 mm in diameter) cut out of the UHMWPE sheets. The holes represented regions of high impedance as no current could flow through those areas. The EIT measurement scheme was then performed again on the damaged samples to obtain a new set of boundary voltage measurements. The relative change in boundary voltage distribution, calculated by subtracting the baseline measurements, was used as input for EIT inverse algorithms for reconstructing conductivity distribution. Here, to evaluate the compatibility of the DAQ hardware with different EIT inverse algorithms, the MATLAB-based iterative Gauss-Newton algorithm (i.e., (4)) and the compressed sensing TwIST algorithm (i.e., (6)) were both implemented for conductivity reconstruction using the DAQ measurements. Their reconstruction resolution was quantified and compared.

E. Edge Intelligence

To transform the traditional EIT data collection and postprocessing workflow, this study further developed an edge computing functionality for the DAQ system. One of the major challenges in deploying the reconstruction algorithm was accessing the Jacobian matrix on the microcontroller, which is the largest set of data needed in the compressed sensing TwIST algorithm. The nRF52840 Feather contains 1024 kB of flash memory and 256 kB of random-access memory (RAM) [45]. Theoretically, the largest Jacobian that the 1024 kB of flash memory could fit, for a 16-electrode setup with 208 voltage measurements, would be a 208 × 1024 matrix corresponding to a 32 × 32 finite element mesh. However, a portion of memory was required to store the main program to operate the DAQ system. For this reason, the size of the Jacobian that could be used for edge computation had to be reduced. Furthermore, rather than storing the Jacobian matrix with on-board memory, it was stored in a commaseparated value (CSV) file on a Secure Digital (SD) card and accessed with an external SD card reader.

To convert the reconstruction algorithm into a microcontroller-compatible library/function, the MATLAB-based compressed sensing TwIST algorithm was first simplified into its essential components relevant to EIT reconstructions (i.e., removing code supporting optional

arguments, removing unnecessary blocks of code, etc.). The simplified algorithm was then converted into a C/C++ function via MATLAB Coder. The converted function required additional modification and optimization since it introduced many redundant loops and utilized standard C/C++ functions that were incompatible with the Arduino library. For example, the optimization process included removing unnecessary arrays that kept track of data as it progressed through the function. These arrays made the code more readable and easier to follow along, but they occupied enormous amounts of contiguous memory that was not available on the microcontroller. Also, as mentioned previously, the Jacobian was stored on an SD card; thus, matrix multiplication with the Jacobian had to be modified to facilitate this. This was achieved by parsing through the Jacobian CSV file, storing individual values in a RAM buffer, and multiplying these values with their respective matrix index.

In addition to the limitation of on-board memory, the lack of computational power could be another challenge. Each iteration of the TwIST algorithm involved multiple instances of performing matrix multiplication with the Jacobian matrix. This could be extremely demanding for a single-core microcontroller, such as the nRF52840 [45]. It should also be noted that using microcontrollers with multiple processing cores could lead to increased power consumption and reduced battery life.

Due to the hardware limitations regarding the lack of memory and computational power, the EIT sensing experiments for evaluating edge intelligence performance were simplified by reducing the number of electrodes on the UHMWPE specimens to an 8-electrode configuration. The finite element mesh was also reduced from the original 96 \times 96 element mesh to an 8 \times 8 element mesh, resulting in a 40 \times 64 Jacobian matrix.

Following the similar test procedures described in Section III.D.3, damages were introduced to the 8-electrode UHMWPE samples, and the corresponding relative change in boundary voltage distribution was used to perform the conductivity reconstruction on the DAQ system. The same reconstruction was also performed on a personal computer (PC) with the original TwIST algorithm as a comparison.

IV. RESULTS AND DISCUSSION

A. Benchmark Testing of the Resistor Network

The resistor network designed for benchmark testing can be simplified into an equivalent resistor between any two nodes based on the concept of series and parallel resistances. The equivalent resistance value could vary, depending on which two electrodes were chosen for measurements. Based on this, the performance of the current source in the DAQ system could be evaluated by characterizing its behavior when subjected to various resistive loads. In addition, by applying the Kirchhoff Voltage Law to the resistor network, it was expected that the voltages at each node would be different. The voltages at each node were measured using the DAQ

system and compared to their theoretical values obtained from LTSpice-based simulations.

Fig. 7(a) shows a configuration where current was injected into A20 and out of A32. The experimental measurements, indicated by the red line in Fig. 7(b), matched closely with those from the simulation, indicated by the blue line. Additional tests were performed with various electrode injection pairs, and the results were consistent across all tested configurations. It should also be noted that there was about a 2.36% error between the theoretical and experimental voltage measurements. This was likely attributed to imperfections in circuitry and/or Joule heating. Overall, the performance of the current source was deemed sufficiently accurate and reliable.

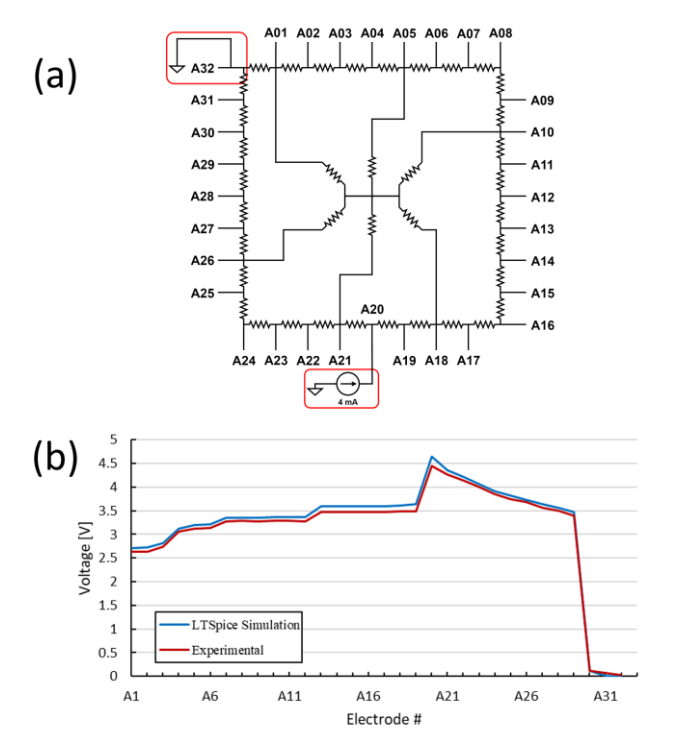


Fig. 7. (a) Resistor network schematic showing current flowing into A20 and out of A32. (b) Experimental voltage distribution measured across all electrodes compared to theoretical values corresponding to (a).

B. Measurement Noise and Kalman Filter-Based Signal Processing

In this study, the noise level in DAQ measurements was quantified using the same resistor network. Fig. 8 shows an example of unfiltered and filtered signals within a one-second time window, represented by the orange and blue lines, respectively. The orange and blue shaded regions highlight the unfiltered and filtered signals' range within two standard deviations, respectively. Here, the vertical axis represents unitless digital values ranging from 0 to 4095, corresponding to a 12-bit resolution ADC. With an analog reference voltage of 3.3 V, each unit of the ADC value corresponds to ~0.8 mV. Upon converting to millivolts, the standard deviations for the unfiltered and filtered signals were 5.32 mV and 0.51 mV,

respectively. In addition, it was found that the signal-to-noise ratio was increased from 66.23 dB to 86.76 dB by applying the Kalman filter, which indicated that the noise in the measured signals was effectively reduced.

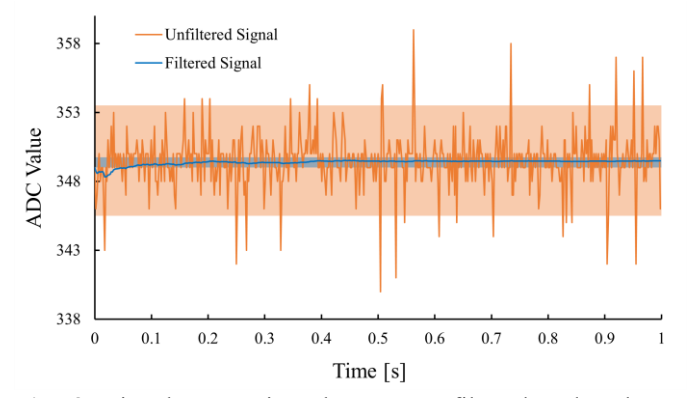


Fig. 8. Signal comparison between unfiltered and Kalmanfiltered ADC measurements within a one-second time window.

C. Comparison Between DAQ Measurements and EIT Forward Problem Simulations

The goal of this comparison is to verify whether the experimental setup using the developed DAQ system along with the conductive UHMWPE as the damage sensing material yields comparable measurements to the EIT forward problem solved with EIDORS. In Fig. 9, the red line represents the voltage measurements from the EIT DAQ system performed on a UHMWPE sample, and the blue line represents the theoretical values calculated from the EIDORSbased forward problem on an assumed homogenous medium. It was found that the experimental measurements obtained using the DAQ system were highly similar to the simulated voltage response, which further confirmed the measurement accuracy and reliability of the DAQ hardware. The minor discrepancies were hypothesized to be due to potential deviations in electrode positioning and electrode contact impedance on the experimental specimens. In addition, the conductivity distribution of pristine UHMWPE samples may

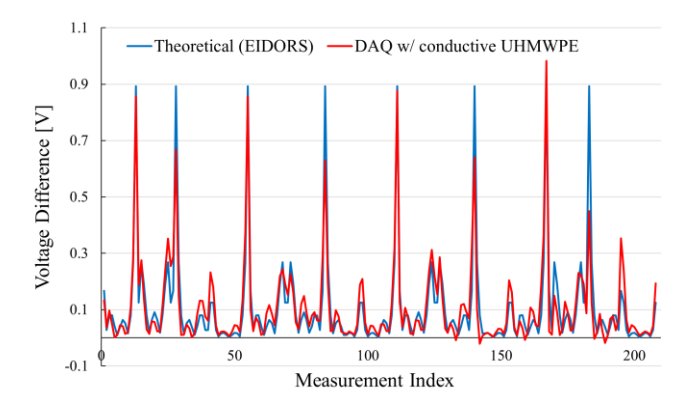


Fig. 9. Experimentally measured boundary voltage distribution of a 16-electrode UHMWPE sample overlapped with the theoretical values simulated from the EIT forward problem on a uniform homogenous material.

not be perfectly uniform as assumed in the EIT forward simulations.

D. Conductivity Distribution Reconstruction of the 16-Electrode Configuration

The first set of EIT damage sensing experiments was conducted on the 16-electrode UHMWPE samples. Here, damages (i.e., holes) were cut out of the material to introduce an area of high impedance at different locations (i.e., four corners) on the samples. The changes in boundary voltage distribution between the damaged and undamaged samples were used as inputs for the EIT reconstruction algorithms, including the iterative Gauss-Newton algorithm and the TwIST algorithm. First, the hyperparameters in the inverse algorithms were selected based on the samples with the most anomalies in each test to achieve the optimal reconstruction of those cases. Then, the selected hyperparameters were used for the remaining reconstructions in each corresponding test. More details on the hyperparameters in the EIT inverse algorithms can be found in [31]. Fig. 10(a) - 10(d) and 10(e) -10(1) show the images of damaged samples and their correspondingly reconstructed conductivity distributions using the two inverse algorithms, respectively. According to the color bars, blue regions in Fig. 10(e) - 10(l) indicate areas of decreased conductivity compared to the baseline conductivity, whereas the red and yellow regions indicate areas of increased conductivity. It was clear that the voltage measurements from the DAQ system could be utilized for both inverse algorithms to detect damages at different locations on the specimens. The locations of reconstructed anomalies also matched well with those of actual damages. To quantify and compare the performance of the two inverse algorithms, the conductivity distributions reconstructed from both were evaluated based on their pixel values. To be more specific, the blur radius was used to rigorously quantify the reconstruction quality and resolution [46], [30], [47]. Here, the blur radius (BR) was defined as

$$BR = \sqrt{\frac{A_R}{A_0}} \tag{11}$$

where A_{θ} is the total sensing area of the domain and A_R is the area with significant changes in reconstructed conductivity. A_R can be quantified by the following expression:

$$A_{R} = \sum_{i=1}^{N} A_{i}$$

$$for all i that \delta \sigma_{i} \ge \frac{1}{2} \max (\delta \sigma_{i})$$
(12)

where N is the total number of elements whose conductivity values are above the threshold. Equations (11) and (12) show that higher resolution reconstructions will lead to a smaller BR value. In other words, reconstructed anomalies with blurred

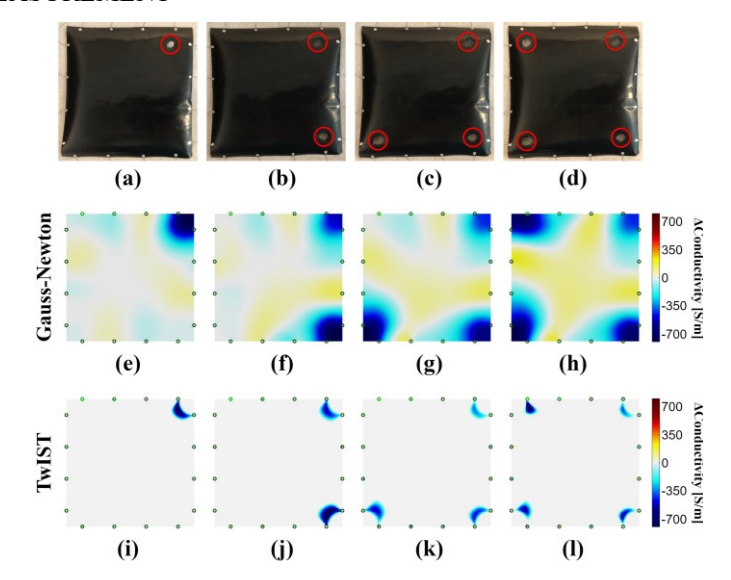


Fig. 10. (a-d) Optical images of a 16-electrode UHMWPE sample with introduced corner damages. Conductivity distributions reconstructed using the (e-h) Gauss-Newton algorithm and (i-l) compressed sensing TwIST algorithm corresponding to the damage scenarios in (a-d), respectively.

features would occupy more area in the sensing domain and vice versa. The calculated blur radii of the two inverse algorithms are shown in Fig. 11.

It can be observed that for all four configurations with anomalies introduced, the images reconstructed with the TwIST algorithm exhibited lower blur radii compared to those reconstructed with the Gauss-Newton algorithm. This was consistent with visual inspection of the reconstruction results (i.e., Fig. 10(e) - 10(h) compared to Fig. 10(i) - 10(l)). In other words, the compressed sensing technique could effectively improve the accuracy and resolution of EIT reconstruction. Therefore, the remaining reconstructions performed in the EIT damage sensing experiments focused on using the compressed sensing TwIST algorithm.

Two additional sets of experiments were also conducted to further evaluate the DAQ system's performance in detecting damage-induced conductivity changes elsewhere on the UHMWPE samples. Fig. 12 and 13 show the reconstructed conductivity maps corresponding to damage scenarios where multiple damages were introduced along the edges and near the central regions, respectively.

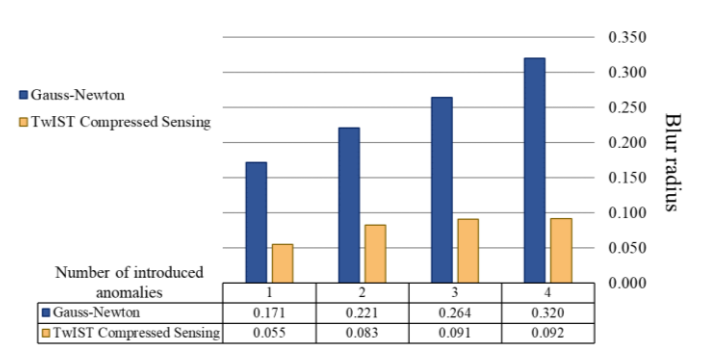


Fig. 11. Comparison between the Gauss-Newton and TwIST compressed sensing algorithms evaluated via blur radius.

While the shapes of the reconstructed anomalies did not perfectly reflect those of the damages on the UHMWPE samples, the locations of the reconstructed anomalies were found to match well. The discrepancies in the reconstructed anomaly shape were hypothesized as artifacts introduced by the reconstruction algorithms when solving the ill-posed EIT inverse problem. Other factors such as measurement noise and imperfections in electrode spacing can also potentially exacerbate the shape discrepancies. Regardless, based on Fig. 10 - 13, one can clearly observe that the data collected from the designed DAQ system, coupled with the compressed sensing TwIST algorithm, could effectively detect damage-induced anomalous conductivity changes at various spatial locations across the sensing domain.

E. Edge Intelligence

In this study, the edge computing functionality was incorporated with the DAQ system to transform the traditional workflow of EIT-based sensing techniques. To address the hardware limitations in memory and computational power, the EIT damage sensing experiments were conducted with fewer number of electrodes (i.e., 8-electrode sample configuration) and a coarser finite element mesh to simplify the inverse reconstruction. The damages were introduced in the same manner as Section IV.D.

Fig. 14(a) - 14(d) and 14(e) - 14(h) show the images of a damaged UHMWPE sample and their corresponding reconstructed conductivity distributions performed using the nRF52840 Feather microcontroller in the DAQ hardware, respectively. It was found that, despite the low resolution, damages could still be detected and spatially located via performing the conductivity reconstruction on an edge device. Also, the reconstruction resolution was arguably sufficient to distinguish each anomaly apart from each other.

Several attempts have been made to improve the reconstruction resolution. Due to the microcontroller's limited memory capacity, a finer mesh utilized more on-board memory for the mutable arrays and repeatedly led to crashes when performing the reconstruction algorithm. Even if there

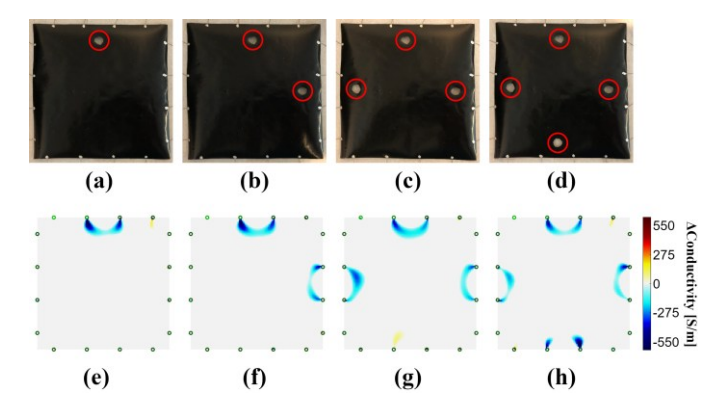


Fig. 12. (a-d) Optical images of a 16-electrode UHMWPE sample with multiple damages on the edges. (e-h) Reconstructed conductivity distributions corresponding to the damage scenarios in (a-d), respectively.

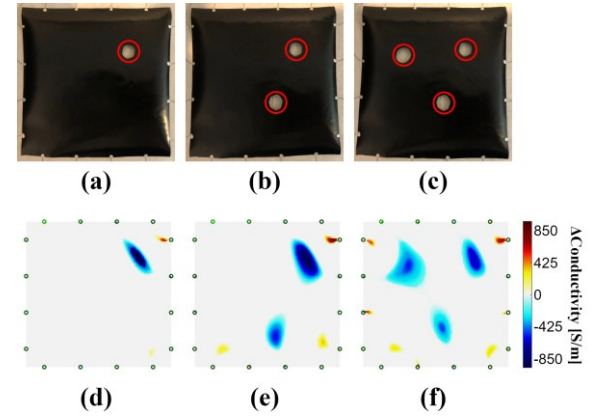


Fig. 13. (a-c) Optical images of a 16-electrode UHMWPE sample with multiple damages near the central regions. (d-f) Reconstructed conductivity distributions corresponding to the damage scenarios in (a-c), respectively.

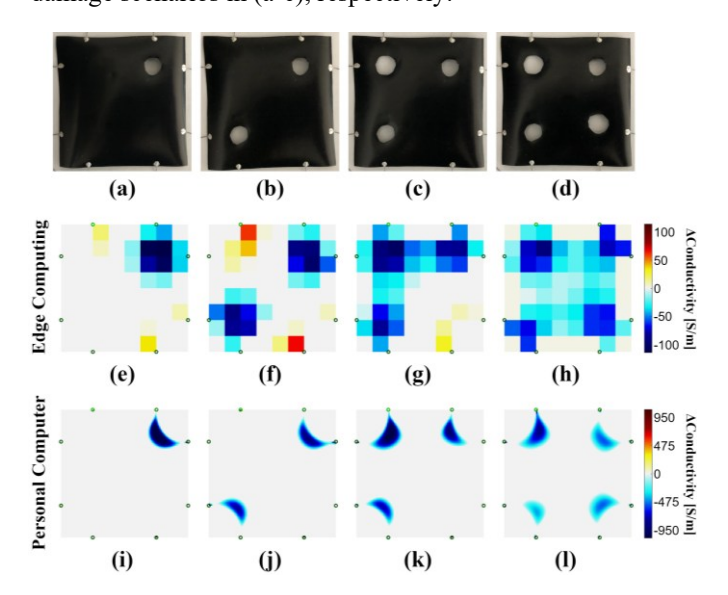


Fig. 14. (a-d) Optical images of an 8-electrode UHMWPE sample with multiple damages on the corners. Conductivity distributions reconstructed with (e-h) the nRF52840 microcontroller and (i-l) a PC corresponding to the damage scenarios in (a-d), respectively.

was sufficient memory, the computational power of the microcontroller further constrained the performance of EIT reconstruction algorithm. For the TwIST algorithm used in this study, it took the microcontroller about seven minutes to complete each reconstruction. This computational time would have increased exponentially with refined mesh resolution. It was found that when performing EIT reconstruction on the edge devices, the most computationally intensive task was matrix multiplication with the Jacobian matrix in the inverse algorithm. The main contributing factor, as previously mentioned in Section III.E, was the fact that the Jacobian needed to be accessed by parsing through a CSV file on an SD card rather than with on-board RAM or flash memory. Therefore, the long reconstruction time suggests that directly adapting traditional, iterative EIT reconstruction algorithms for low-computational edge devices may not be a viable

solution for real-time analysis. As a potential future direction to enhance the EIT edge computing performance, one may develop more efficient EIT algorithms to better accommodate the limited computational capacity of edge devices.

To demonstrate that the data collected using the DAQ system for this 8-electrode sample configuration was still of high quality, the voltage measurements were further processed using a PC (i.e., with sufficient hardware memory and computational capacity) for comparison. The same mesh size as Section IV.D was used here for the reconstruction. Fig. 14(i) - 14(l) show the reconstructed conductivity distributions corresponding to the multiple damages, where the detected anomalies were highly defined. The position of each anomaly also matched very well with those in the UHMWPE samples. This indicated that the data collected from the DAQ system was reliable and accurate, and the relatively low quality of reconstruction results shown in Fig. 14(e) - 14(h) indeed resulted from the edge device's computational capacity.

V. CONCLUSION

This study aims to transform the traditional workflow for EIT measurement and data processing with a novel, highperformance DAQ system. The EIT DAQ system developed in this study featured compact footprint, high portability, wireless communication, low cost, interfacing smartphone, versatility for various electrode configurations, and edge intelligence functionality. Benchmark tests were performed by comparing the DAQ measurements with circuitry simulation and EIT forward problem simulation. The DAQ hardware was demonstrated capable of obtaining stable and accurate voltage measurements. To enhance the signal quality for ensuring reliable EIT inverse reconstruction, an optimized Kalman filter was implemented to process the raw measurements, which effectively reduced the noise level. Then, the DAQ system was coupled with EIT inverse algorithms, including the iterative Gauss-Newton and compressed sensing TwIST algorithms, to perform a series of damage detection experiments. spatial measurements were compatible with both reconstruction algorithms, but the compressed sensing algorithm showed higher reconstruction resolution and accuracy, which was consistent with the theory. In addition, to achieve the novel edge computing function, the compressed sensing algorithm was compiled into a C/C++ library and implemented onto the microcontroller in the DAQ system. EIT sensing experiments showed that the conductivity distribution of the material of interest could be successfully reconstructed on the DAQ system itself (without using an external PC).

It became apparent that modifying traditional, iterative EIT reconstruction algorithms for edge deployment may not have been the most effective solution. Future research will investigate alternative approaches to perform EIT conductivity reconstruction more efficiently on the microcontroller to overcome the current limitations associated with on-board memory and computing capacity. One possible approach is to implement machine learning/artificial intelligence-based reconstruction algorithms onto the EIT edge devices. Also,

other capacities of EIT edge intelligence will be investigated, such as damage identification and damage severity classification. In addition, regarding the DAQ hardware itself, additional efforts will be made to further reduce its spatial footprint.

Overall, this study represents a crucial step for advancing the development of high-performance EIT DAQ systems with edge intelligence for applications in structural health monitoring and wearable/implantable technologies.

ACKNOWLEDGMENT

This research was supported by the U.S. National Science Foundation under grant no. 2138756.

REFERENCES

- 1. Brown, B.H., *Electrical impedance tomography (EIT): a review.* Journal of Medical Engineering & Technology, 2003. **27**(3): p. 97-108.
- 2. Liliana, B., *Electrical impedance tomography*. Inverse Problems, 2002. **18**(6): p. R99.
- 3. Zou, Y. and Z. Guo, *A review of electrical impedance techniques for breast cancer detection.* Medical Engineering & Physics, 2003. **25**(2): p. 79-90.
- Sun, B., et al., An Improved Tikhonov Regularization Method for Lung Cancer Monitoring Using Electrical Impedance Tomography. IEEE Sensors Journal, 2019. 19(8): p. 3049-3057.
- 5. Cherepenin, V., et al., *A 3D electrical impedance tomography (EIT) system for breast cancer detection.* Physiological Measurement, 2001. **22**(1): p. 9.
- 6. Zhu, Z., H.S. Park, and M.C. McAlpine, *3D printed deformable sensors*. Science Advances. **6**(25): p. eaba5575.
- 7. Hu, C.-L., et al. *Dry Wearable Textile Electrodes for Portable Electrical Impedance Tomography*. Sensors, 2021. **21**, DOI: 10.3390/s21206789.
- 8. Wang, L., et al., Corona-Enabled Electrostatic Printing for Ultra-fast Manufacturing of Binder-Free Multifunctional E-Skins. ACS Applied Materials & Interfaces, 2021. **13**(38): p. 45966-45976.
- 9. Zhang, Y. and C. Harrison, *Tomo: Wearable, Low-Cost Electrical Impedance Tomography for Hand Gesture Recognition*. 2015. 167-173.
- Hong, S., et al., A 10.4 mW Electrical Impedance Tomography SoC for Portable Real-Time Lung Ventilation Monitoring System. IEEE Journal of Solid-State Circuits, 2015. 50(11): p. 2501-2512.
- 11. Martins, T.d.C., et al., *A review of electrical impedance tomography in lung applications: Theory and algorithms for absolute images.* Annual Reviews in Control, 2019. **48**: p. 442-471.
- 12. Tomicic, V. and R. Cornejo, Lung monitoring with electrical impedance tomography: technical considerations and clinical applications. J Thorac Dis, 2019. 11(7): p. 3122-3135.
- 13. Shi, X., et al., *High-Precision Electrical Impedance Tomography Data Acquisition System for Brain Imaging.*IEEE Sensors Journal, 2018. **18**(14): p. 5974-5984.

- 14. Jiang, Y.D. and M. Soleimani, *Capacitively Coupled Electrical Impedance Tomography for Brain Imaging*. IEEE Transactions on Medical Imaging, 2019. **38**(9): p. 2104-2113.
- 15. Aristovich, K.Y., et al., *Imaging fast electrical activity in the brain with electrical impedance tomography.*NeuroImage, 2016. **124**: p. 204-213.
- 16. Wang, L., et al., *Distributed Pressure Sensing Using Carbon Nanotube Fabrics*. IEEE Sensors Journal, 2016. **16**(12): p. 4663-4664.
- 17. Yao, J., et al., Development of a Wearable Electrical Impedance Tomographic Sensor for Gesture Recognition With Machine Learning. IEEE Journal of Biomedical and Health Informatics, 2020. **24**(6): p. 1550-1556.
- Tallman, T.N., et al., Damage detection via electrical impedance tomography in glass fiber/epoxy laminates with carbon black filler. Structural Health Monitoring, 2014. 14(1): p. 100-109.
- 19. Hao, F., et al., Carbon-Nanotube-Film-Based Electrical Impedance Tomography for Structural Damage Detection of Carbon-Fiber-Reinforced Composites. ACS Applied Nano Materials, 2021. 4(5): p. 5590-5597.
- Rocha, H., et al., Damage localization on CFRP composites by electrical impedance tomography. Materials Today Communications, 2022. 32: p. 104164.
- 21. Cagáň, J. and L. Michalcová, Impact Damage Detection in CFRP Composite via Electrical Resistance Tomography by Means of Statistical Processing. Journal of Nondestructive Evaluation, 2020. 39(2): p. 38.
- 22. Hallaji, M. and M. Pour-Ghaz, A new sensing skin for qualitative damage detection in concrete elements: Rapid difference imaging with electrical resistance tomography. NDT & E International, 2014. **68**: p. 13-21.
- 23. Hallaji, M., A. Seppänen, and M. Pour-Ghaz, *Electrical impedance tomography-based sensing skin for quantitative imaging of damage in concrete*. Smart Materials and Structures, 2014. **23**(8).
- 24. Hou, T.-C. and J.P. Lynch, Electrical Impedance Tomographic Methods for Sensing Strain Fields and Crack Damage in Cementitious Structures. Journal of Intelligent Material Systems and Structures, 2008. 20(11): p. 1363-1379.
- McAlorum, J., et al., ConcrEITS: An Electrical Impedance Interrogator for Concrete Damage Detection Using Self-Sensing Repairs. Sensors (Basel), 2021. 21(21).
- Rintoul, J. Documentation and Tutorials for OpenEIT.
 2018 [cited 2023 Aug 23].
- 27. Zhang, Y.a.X.R.a.H.C., Advancing Hand Gesture Recognition with High Resolution Electrical Impedance Tomography, in Proceedings of the 29th Annual Symposium on User Interface Software and Technology. 2016, Association for Computing Machinery. p. 843–850, numpages = 8.
- 28. Shi, W.a.D.S., *The Promise of Edge Computing*. Computer, 2016. **49**(5): p. 78-81.
- 29. Abolfazl Roshanpanah and Mahdi Abbasi and Hani Attar and Ayman Amer and Mohammad, R.K.a.A.A.S., *An Electrical Impedance Imaging System Towards Edge Intelligence for Non-Destructive Testing of Concrete.*

- Tsinghua Science and Technology, 2024. **29**(3): p. 883-896.
- 30. Wang, L., Development of multifunctional nanocomposite sensing systems for structural and human health monitoring, in Structural Engineering. 2019, University of California San Diego: San Diego, California. p. 161.
- 31. Zhao, Y., et al., Comparison of electrical impedance tomography inverse solver approaches for damage sensing, in Smart Structures and Materials + Nondestructive Evaluation and Health Monitoring. 2017, Society of Photo-Optical Instrumentation Engineers (SPIE): Portland, Oregon, United States.
- 32. Wang, L., et al., *Nanocomposite Fabric Sensors for Monitoring Inflatable and Deployable Space Structures*. 2016. V001T05A006.
- 33. Wang, Q., et al., Reconstruction of electrical impedance tomography (EIT) images based on the expectation maximum (EM) method. ISA Trans, 2012. 51(6): p. 808-20.
- 34. Tehrani, J.N., et al. A comparison between compressed sensing algorithms in Electrical Impedance Tomography. in 2010 Annual International Conference of the IEEE Engineering in Medicine and Biology. 2010.
- Bioucas-Dias, J.M. and M.A.T. Figueiredo, A New TwIST: Two-Step Iterative Shrinkage/Thresholding Algorithms for Image Restoration. IEEE Transactions on Image Processing, 2007. 16(12): p. 2992-3004.
- 36. Lady, A. Introducing the Adafruit nRF52840 Feather. 2019.
- 37. Devices, A., ADG726/ADG732: Analog Multiplexers Data Sheet (Rev. C). 2006, Analog Devices.
- 38. Cunningham, C., et al. Bluefruit LE Connect for iOS and Android. 2015.
- 39. Afaneh, M. Bluetooth Low Energy (BLE): A Complete Guide. 2022.
- 40. Zhang, L. and H. Wang. Single source current drive patterns for electrical impedance tomography. in 2010 IEEE Instrumentation & Measurement Technology Conference Proceedings. 2010.
- 41. van Biezen, M., *The 3 Calculations Of The Kalman Filter*, in *The Kalman Filter*. 2016: iLectureOnline.
- 42. Sene, D., *SimpleKalmanFilter*, MajorArkwolf, EdJoPaTo, and IanSC, Editors. 2016, GitHub.
- 43. Doblinger, G. An adaptive Kalman filter for the enhancement of noisy AR signals. in ISCAS '98.

 Proceedings of the 1998 IEEE International Symposium on Circuits and Systems (Cat. No.98CH36187). 1998.
- 44. Adler, A. and W.R. Lionheart, *Uses and abuses of EIDORS: an extensible software base for EIT.* Physiol Meas, 2006. **27**(5): p. S25-42.
- 45. Infocenter, N.S., nRF52840 Product Specification. 2021, Nordic Semiconductor.
- 46. Huang, J.-J., et al., *Design of wearable and wireless electrical impedance tomography system*. Measurement, 2016. **78**: p. 9-17.
- 47. Graham, B.M. and A. Adler, *Objective selection of hyperparameter for EIT*. Physiol Meas, 2006. **27**(5): p. S65-79.